Electronic Supplementary Information

A 3D hierarchical porous adsorbent constructed by cryo-polymerization for ultrafast uranium harvesting from seawater

Dagang Li[a], Yaozu Liao[b, *], Zheng Chen[c, d], Xixin Chang[e], Xu Zhang[a], Chongcheng Chen[c,d], Chang Cui[a], Zilei Zhang[a], Constantin Muhire[a], Weiwu Tang[a], Dongxiang Zhang[a, *], Jinying Li[a,f] and Xiyan Xu[a, *]

[a]School of Chemistry and Chemical Engineering, Beijing Institute of Technology, Beijing 102488, China

[b]State Key Laboratory for Modification of Chemical Fibers and Polymer Materials, Donghua University, Shanghai 201620, China

[c]School of New Materials and Shoes & Clothing Engineering, Liming Vocational University, Quanzhou 362000, Fujian, China

[d]Applied Technology Engineering Center of Fujian Provincial Higher Education for Practical Chemical Material, Quanzhou 362000, Fujian, China

[e]CNNC Key Laboratory on Uranium Extraction from Seawater, Beijing Research Institute of Chemical Engineering and Metallurgy, Beijing 101149, China

[f]China National Nuclear Corporation, Beijing 100822, China

* Corresponding Authors:

Dr. Dongxiang Zhang (e-mail: boris@bit.edu.cn); Dr. Xiyan Xu (xiyanxu@bit.edu.cn) and Dr. Yaozu Liao (yzliao@dhu.edu.cn);

Phone: (86) 010-68941331

Fax: (86) 010-68914503

Contents

Figure S21. Distribution coefficient K_d and ion species.

Figure S22. Schematic diagram of natural seawater adsorption.

Figure S23. Comparison of average adsorption rates in natural seawater for 7 days.

Figure S24. Adsorption of uranium in natural seawater by PAA-PAO and PEI-PAA-PAO.

Figure S25. A large-size adsorbent with a size of 33 cm × 28 cm × 0.5 cm and a picture of uranium extraction from seawater were prepared.

Table S1. Mass concentrations corresponding to cryo-crystallization curve experiment.

Table S2. Relationship between composition of polymerization system and adsorbent forming.

Table S3. Results of pseudo first-order model, pseudo second-order model and intra-particle model parameter fitting.

Table S4. Parameter fitting results of isothermal models.

Table S5. ESP simulation results of uranium interaction with adsorbent.

Table S6. Initial ion species and concentration in selectivity experiment of multi-ion adsorption.

Table S7. Comparation this work with other adsorption materials.

Supplementary movie1. Demonstration of simulated seawater infiltration and uranium interception.

Supplementary movie2. 3D reconstruction and continuous connected pores.

Supplementary movie3. Contact angle experiment.

Supplementary movie4. Compression recovery.

Supplementary movie5. Strength demonstration.

Supplementary movie6. Adsorption demonstration.

Supplementary movie7. Desorption demonstration.

Materials and pretreatment.

Acrylic acid (AA) (99 %) and acrylonitrile (AN) (99 %) were purchased from Sinopharm Chemical Reagent Co., LTD., China. Benzoyl peroxide (BPO) (98.5 %), N, N'-dimethylaniline (DMA) (99 %), dimethyl sulfoxide (DMSO) (99 %), Glycol dimethacrylate (98 %) (EGD) and polyurethane (PU) (M_w = 120 000 g mol^{-1}) were purchased from Macklin Reagent Co., LTD., China. Polyethylene imide (PEI) (M_w =600 g mol^{-1}), 1-ethyl-3 -(3-dimethylaminopropyl) carbon diimide (EDC) (99 %), N-hydroxysuccinimide (NHS) (99 %), salicylaldehyde (98.5 %) were purchased from Anergy Chemical Co., LTD., China. Ethanol (100 %), HCl (37 %), Potassium bromide (chromatographic pure), activated carbon, H_2O_2(30 %), HNO_3 (99 %), $NaCO_3$(99 %) purchased from Xilong Chemical Co., LTD., China. Uranyl nitrate hexahydrate (99 %) purchased from RHAWN, China. Sodium metavanadate (99 %), Manganese nitrate tetrahydrate (98 %), Calcium nitrate tetrahydrate (99 %), Nickel nitrate (99 %) and Copper nitrate (98 %) and Zinc nitrate hexahydrate (99 %) purchased from Xilong Chemical Co., LTD., China; Cobaltous nitrate hexahydrate (99 %) and Ferric nitrate nine hydrate (98 %), purchased from Sinopharm Chemical Reagent Co., LTD., China. The liquid AA raw material was statically adsorbed on activated carbon for 24 h to remove the polymerization inhibitor. AN was purified by negative pressure distillation at 60~70℃. BPO can be used only after secondary recrystallization. PU was dissolved in DMSO at 90 ℃ and prepared into 13.00 % PU/DMSO solution, cooled to room temperature for use. BPO was prepared in 5 % BPO/DMSO solution with DMSO as solvent. DMA was prepared with a 3 % DMA/DMSO solution as a solvent.

Methods

Cryo-crystallization curve mapping.

When the solution is cooled to a certain temperature, the solvent will crystallize and the corresponding temperature is the freezing point temperature (θ_s, ℃). The solvent continues to crystallize and releases latent heat (I, J mol^{-1}) from liquid phase to solid phase, so that the temperature of the system will suddenly surge, and the release of latent heat and the heat conduction of the environment will temporarily balance. Therefore, the temperature after temperature increase will be in a short time equilibrium state, the highest point of temperature increase is the crystallization state of all solvents, and the temperature at this point is defined as the crystallization temperature (θ_c, ℃). Cyro-crystallization curve drawing BPO and DMA were removed from the polymerization system and only the reaction materials were retained for determination. Homogenized AA, AN, EGD, PU and DMSO into a mixed solution, and poured 0.5 g of mixed solution into cylindrical silica gel mold (outer diameter is 5 mm, wall thickness is 1 mm and height is 40 mm). A t thermocouple (wrnk-161 Shanghai specific electron, China) with a temperature range of -200 ℃ ~ 1000 ℃ was inserted into the liquid of the silica gel mold, which was stable for 30 min under the condition of 20 ℃ water bath, and this was used as the starting temperature for drawing the cryo-crystallization curve. After that, the silica gel mold was inserted into the cryogenic constant temperature tank into the freezing equipment (THCD-01, Ningbo Tianheng, China) with ethanol atmosphere of -20 ± 0.5 ℃, -25 ± 0.5 ℃ and -30 ± 0.5 ℃ respectively, and the thermal resistance was used to record the temperature of the polymerization system every 5 s to obtain the cryo-crystallization curve. The cryo-crystallization curves of solutions with different mass concentrations were measured according to the ratio in **Table S1**. Each test was determined 3 times in parallel. The cyro-crystallization curves of DMSO pure solvent were used as calibration. The initial temperature of the cryo-crystallization curve of DMSO pure solvent was determined to be 20 ℃, and its calibration freezing point temperature was 18.1 ± 0.2 ℃ (**Fig. 1A, a**).

Synthesis of PAA-PAN.

At 20 ℃, 0.3534 g AA, 0.4527 g AN, 0.0412 g EGD and 0.7121 g BPO/DMSO solution were successively poured into 4.0972 g DMSO solvent under magnetic stirring to form a homogeneous solution. Continue stirring 3.5672 g PU/DMSO solution was added to the mixed solution and stirred continuously for 1 h. Then,

0.7762 g DMA/DMSO solution was added to the above-mentioned solution, and the reaction solution was quickly stirred to form a uniform reaction solution, and poured into the silica gel mold with a size of 20 mm × 50 mm × 5 mm (mold wall thickness 0.2 mm). The mold was slowly immersed in ethanol which was pre-cooled to -20 ± 0.5 ℃, and ethanol was used to achieve rapid cryo-crystallization of the solvent in the whole reaction solution. The polymerization was maintained at -20 ± 0.5 ℃ for 18 h. After polymerization, the crystallized polymer was removed from the silica gel mold at the temperature of -25 ℃ ± 0.5 ℃ and directly immersed in ethanol. After 12 h, the DMSO solvent in the polymer was replaced by ethanol, and then the polymer was soaked and washed by deionized water for 3 to 4 times at room temperature to obtain PAA-PAN. During the freezing process, solvent crystals form, and soluble substances that can aggregate are "squeezed" into the non-crystalline regions (**Scheme. 1Ae**) through crystallization. Subsequently, the copolymerization reaction of AN and AA is triggered by an oxidation-reduction reaction, forming a semi-interpenetrating network of polymer (**Scheme. 1Af**). After the reaction is taken out, the ice crystal melts and leaves "supemacropores" in place. The strong hydrophobic interaction between the PU side chains forms a physical crosslinking structure between the PU molecular chains, which promotes the polymer skeleton prepared by polymerization to become a double network structure (**Scheme. 1Ah**).

Synthesis of sy-PEI-PAA-PAO.

The synthesis of sy-PEI-PAA-PAO was described using 1.0000 g PAA-PAN as the reference material. 1.0000 g PAA-PAN was added to aqueous solutions with 6.234 % EDC and 3.156 % NHS 20.000 g. After ultrasonic mixed at 20 ℃ for 30 min, 1.0326 g PEI was added to the reaction system in ice water bath until PEI dissolved completely. Ultrasonic reaction system for 20 min. The PAA-PAN grafted with PEI was reacted at 60 ℃ water bath for 5 h and named PEI-PAA-PAN. Grafting rate was calculated by formula (1)[1]. Under this condition, the grafting rate of PEI was 92.82 ± 2.72 %. PEI-PAA-PAN was placed in 10 mL ethanol, and 1.0234 g salicylaldehyde was dropped into ethanol at 65 ℃ for 30 min to form a yellow solution. After 5 hours of reaction, Schiff base was obtained, named sy-PEI-PAA-PAN. It was washed with ethanol for 3 ~ 4 times to remove unreacted salicylaldehyde. The grafting rate of sy-PEI-PAA-PAN salicylaldehyde was 87.63 ± 2.32 % according to equation (1). sy-PAI-PAA-PAO was obtained from aqueous solution of methanol-water (1:1 by volume ratio) with 24.34 % hydroxylamine hydrochloride and 19.11 % sodium

carbonate in water bath at 70 ℃ for 5 h. PAA-PAO and PEI-PAA-PAO were obtained by reacting PAA-PAN and PEI-PAA-PAN, respectively, with a hydroxylamine hydrochloride solution with a mass fraction of 25.56 % and a sodium carbonate solution with a mass fraction of 25.56 % in a methanol-water (volume ratio of 1:1) solution at 70 ℃ in a water bath for 5 h.

$$\varphi_g = \frac{m_1 - m_0}{m_0} \times 100\% \quad \text{(eq1)}$$

Where, φ_g represents the grafting rate (%), m_1 (g) and m_0 (g) represent the absolute dry mass of polyacrylic acid before and after grafting, respectively.

Due to the amidoxime groups only come from acrylonitrile, and the salicylaldehyde Schiff base only comes from the transformation of acrylic acid. Therefore, the ratio of amidoxime groups to salicylaldehyde Schiff bases can be approximately expressed by the mass ratio of AN to AA in the polymerization reaction system.

Characterization.

The hierarchical porous adsorbents were naturally dried in air, then placed in an 80 ℃ oven (dzf-6050, Suzhou Jiangdong Precision Instrument Co., Ltd. China) for 4 h, then sampled and observed the micro morphology by scanning electron microscope (SEM) (JSM-7500f, JEOL, Japan), analyzed the surface elements of the adsorbent (EDS) and scanned the Mapping image. X-ray diffraction (XRD) was used to test the object image and crystal structure of the samples (Ultima IV, RIGAKU, Japan), and X-ray photoelectron spectroscopy (XPS) (ESCALAB 250XI, Thermo Fisher, USA) was used to test the full spectrum scanning of elements before and after adsorption on the solid surface of the adsorbent and the high-resolution scanning of U, C, N, O elements. Fourier transform infrared spectroscopy (FT-IR) (irprestige-21, Shimadzu, Japan) tested the functional group characteristics of various types of polymers. 3 mg~6 mg of absolute dry solid sample was analyzed the thermogravimetry with thermogravimetric analyzer (STA 449f3, Netzsch, Germany). The temperature test range was 30 ℃ ~700 ℃, N_2 atmosphere, and the heating rate was 10 ℃ min^{-1}. The hydrophilicity of adsorbent was determined by the dynamic contact angle of pure water droplets on the solid surface with the contact angle meter (JC200d Zhongchen digital technology, China), and 3 parallel tests were carried out. A 3D X-ray micro-computed tomography (microCT) was used to visualize and reconstruct the 3D

structure of sy-PEI-PAA-PAO adsorbent (ZEISS Xradia 520 Versa, USA), source-RA distance=12 mm and detector-RA distance = 15 mm. The physical size of volume was 1016 μm (*x*-axis) ×1003 μm (*y*-axis) × 993 μm (*z*-axis). The voltage was 50 kV, power was 4 W, obtained 1002 SEM images. The adsorbent 3D image and pore structure analysis were reconstructed visually with "Avizo" 3D visualization software. Specific surface areas were tested by N_2 adsorption method through BET analyzer (ASAP 2020, Micromeritics, USA). The mercury intrusion test method (MicroActive AutoPore V 9600, USA) obtained supermacro pores size and only supermaropore adsorbent specific surface area.

Compression performance tests.

The compressive properties of different types of materials were tested after they were fully wetted in pure water. Cylindrical samples with diameter × height =10 mm×10 mm was prepared in a silica gel mold obtained from different formulations. The sample was placed in the material mechanics testing equipment (UTM2502, SZ Technology, China) for compression test. In the test, the compression rate was controlled at 1 mm min^{-1}, and the compression was terminated when the compression strain of all samples was 0.7 mm /mm, and the compression stress and strain were recorded. 3 samples were prepared in parallel for each sample and tested for 3 times in parallel. The average value of compressive stress [σ_c (MPa)]-strain [ε_c (mm/mm)] curve was obtained[2].

Adsorption test.

Three different solution matrices were selected for different research targets in the current work, including a uranium solution in deionized water, a mixed heavy metal ion solution based on multiple ion configurations in seawater, and real natural seawater. Uranyl nitrate hexahydrate was dissolved in ultrapure water and prepared into adsorption solution with uranium mass concentration of 28 mg g^{-1}, 20 mg g^{-1} and 12 mg g^{-1} [3-6]. The pH of the adsorption solution was adjusted by 0.1 mol L^{-1} HNO_3 and 0.1 mol L^{-1} $NaCO_3$ solution, and the pH was measured by a pH meter (FE20K pH meter, Mettler Toledo USA). sy-PEI-PAA-PAO adsorbent with a liquid-solid mass ratio of 1:0.03 (L g^{-1}) was added to uranium aqueous solutions with different mass concentrations and placed in an oscillator (STIK PSE-T150A Shidukai Instrument Equipment Co., LTD., China). Static adsorption was performed at a vibrating speed of 150 r min^{-1}. The adsorption effect of sy-PEI-PAA-PAO adsorbent on uranium was investigated. 1 mL solution was taken out at a certain interval, and its mass

concentration was detected by arsenazo (iii) as the display agent and the absorbance was detected by visible spectrophotometry at the absorption wavelength of 652 nm[7, 8] (T9, BEIJINGPUXI, China). The adsorption capacity of uranium in the sample was calculated as presented in Equation (2). Three parallel tests were conducted. According to *ref.*[9-11], V, Zn, Mn, Cu, Fe, Ni, Co, Ba and U were added into 500 mL conical bottles respectively. Initial mass concentrations of all ions are presented in **Table S6**, and the pH was adjusted to 8.0 ± 0.2. The adsorption temperature was 298.15 K and the adsorption time was 36 h. Three tests were performed in parallel. The adsorption properties of the adsorbent under the condition of multi-ion coexistence were investigated. The ion blend was detected by ICP-MS (I-CAP RQ Thermo Fisher USA) to test the ion mass concentration after adsorption.

$$Q = V \times \frac{\rho_0 - \rho}{m} \quad \text{(eq2)}$$

where ρ_0 (mg L^{-1}) is the initial mass concentration of uranium, ρ (mg L^{-1}) is the mass concentration corresponding to adsorption to a certain point, V (L)is the volume of uranium solution, Q (mg g^{-1}) is the adsorption capacity, and m (g) is the dry weight of sy-PEI-PAA-PAO.

Desorption.

The sy-PEI-PAA-PAO adsorbent, which had adsorbed uranium, was placed in a mixed solution of 0.15 mol L^{-1} H_2O_2 and 1 mol L^{-1} Na_2CO_3 with a volume of 200 mL as the eluent[12]. The desorption test was conducted by applying a constant temperature shock of 50 ℃. After a 2-hour desorption period, the mass concentration of uranium in the water was detected and the desorption rate (%) was calculated using equation (3).

$$\psi = \frac{Q_d}{Q} = \frac{\rho_d \times V_d}{m \times Q} \times 100\% \quad \text{(eq3)}$$

Where ψ (%) is the desorption rate, Q_d (mg g^{-1}) is the desorption capacity, ρ_d (mg L^{-1}) is the mass concentration of uranium in the aqueous phase after desorption, V_d (L) is the volume of desorption liquid.

Adsorption kinetics.

The fixed adsorption temperature was 298.15K, and the adsorption force was determined according to the relationship between adsorption time and adsorption capacity. Pseudo-first-order kinetic equation and pseudo-second-order kinetic equation was applied to fit the adsorption process, and the intra-particle equation was

used to fit the adsorption process to determine the diffusion properties in the adsorption process. The pseudo-first-order dynamic equation and the pseudo-second-order dynamic equation are presented in Equation (4) and (5), and the intra-particle equation is presented in Equation (6).

$$\ln\left(\frac{Q_e}{Q_e - Q}\right) = k_1 \times t \quad \text{(eq4)}$$

$$\frac{t}{Q} = \frac{1}{k_2 \times Q_e^2} + \frac{t}{Q_e} \quad \text{(eq5)}$$

$$Q = k_p \times t^{0.5} + C \quad \text{(eq6)}$$

Where Q (mg g^{-1}) is the adsorption capacity corresponding to adsorption time t (h) at a certain time, k_1 (h^{-1}) is the first-order kinetic rate constant, k_2 [g $(mg \cdot h)^{-1}$] is the second-order kinetic rate constant, k_p [mg $(g \cdot h^{0.5})^{-1}$] is the internal diffusion coefficient, and C (mg g^{-1}) is a constant.

Adsorption phase equilibrium.

We arranged the initial mass concentration of 10 mg L^{-1} ~ 200 mg L^{-1}, determined the relationship between equilibrium adsorption capacity and equilibrium mass concentration at 298.15 K, 308.15 K, 318.15 K temperature and obtained the phase equilibrium curves, respectively. Langmuir, Freundlich, Temkin, Sips, Toth and Redlich-Peterson isotherm models were used to fit the adsorption equilibrium curves. The specific forms of Langmuir, Freundlich, Temkin, Sips, Toth and Redlich-Peterson isotherm models are shown in Equations (7) to (12), respectively. For Langmuir model, the separation factor R_L can be used to judge whether the adsorption process of uranium is favorable or not. If the value of R_L is between 0 and 1, it indicates a favorable adsorption process. The calculation of R_L is obtained by equation (13). For the multi-ion adsorption system, the distribution coefficient K_d can be calculated by equation (14), and the selectivity of different ions and uranium $S_{U/M}$ can be calculated by equation (15).

$$Q_e = \frac{Q_\infty \times b_L \times \rho_e}{1 + b_L \times \rho_e} \quad \text{(eq7)}$$

$$Q_e = K_F \times \rho_e^{\frac{1}{n}} \quad \text{(eq8)}$$

$$Q_e = \frac{RT}{b} \ln(A\rho_e) \quad \text{(eq9)}$$

$$Q_e = \frac{Q_m K_S \rho_e^{\alpha}}{1 + K_S \rho_e^{\alpha}} \quad \text{(eq10)}$$

$$Q_e = \frac{K_T \rho_e}{\left(a_T + \rho_e^{\beta}\right)^{\frac{1}{\beta}}} \quad \text{(eq11)}$$

$$Q_e = \frac{K_{RP} \rho_e}{1 + a_{RP} \rho_e^{\gamma}} \quad \text{(eq12)}$$

$$R_L = \frac{1}{1 + b_L \times \rho_0} \quad \text{(eq13)}$$

$$K_d = \frac{Q_e}{\rho_e} \quad \text{(eq14)}$$

$$S_{U/M} = \frac{K_d(U)}{K_d(M)} \quad \text{(eq15)}$$

Where Q_∞ (mg g^{-1}) is the theoretical saturated adsorption capacity of the adsorbent, b_L (L mg^{-1}) is the Langmuir adsorption coefficient, K_F [$(mg^{\frac{n-1}{n}} \cdot L^{\frac{1}{n}}) \cdot g^{-1}$] is the Freundlich adsorption coefficient, n is the adsorption constant, and Q_e (mg g^{-1}) is the equilibrium adsorption capacity corresponding to the equilibrium mass concentration ρ_e (mg L^{-1}). T(K) is the adsorption temperature, R is a thermodynamic constant, 8.315 J $(mol \cdot K)^{-1}$, b [$(J \cdot g)$ $(mol \cdot mg)^{-1}$] and A (L mg^{-1}) are Temkin isotherm model parameters. Q_m(mg g^{-1}) is Sips theoretical maximum adsorption capacity. K_S [$(L\ mg^{-1})^{\alpha}$] and α are Sips isotherm model parameters. K_T (mg g^{-1}), a_T [$(mg\ L^{-1})^{\beta}$] and β are Toth isotherm model parameters. K_{RP} (L g^{-1}), a_{RP} [$(L\ mg^{-1})^{\gamma}$] and γ are Redlich-Peterson isotherm model parameters.

Natural seawater adsorption.

Natural seawater was taken from the East China Sea in Quanzhou, Fujian Province, China (119°07' E, 24°89' N). Adsorption process was tested through the flowsheet presented in **Supplementary Fig. 18**. Uranium in seawater was spiked to an initial concentration of (3.33 ± 0.02) × 10^{-3} mg L^{-1}. The ambient temperature was controlled at 298.15 K. The pH of seawater was 7.9 ± 0.2, and the circulating flow of seawater was adjusted to 70 mL min^{-1}. The ratio of the total volume of seawater to the amount of adsorbent was controlled as 10^4:1 (L g^{-1}). The mass concentration of uranium element was detected by ICP-MC in seawater, and the adsorption amount of uranium element was calculated by Equation (2). Three parallel experiments.

Antibacterial testing.

The solid and liquid culture media, tubes, and test materials were sterilized for 1.5 h in an autoclave. In the sterile environment, two sterile tubes were taken, and an equal amount of liquid culture medium was added to each, followed by the addition of 8 μL of the bacterial strain, which was shaken well. The test sample (the other tube served as a control) was added to one of the tubes and placed in a 37 ℃ bacterial incubator for 5 h. The solid culture medium was poured into two culture dishes to form solid culture media, and the culture media obtained after the above cultivation were uniformly spread on the surface of the solid culture medium. After sealing, they were placed in a 37 ℃ incubator for 12 h and the antibacterial effect was tested by measuring the number of colonies. In addition, a test sample of approximately 0.5 cm in size was added to the surface of the solid culture medium, sealed, and placed in a 37 ℃ incubator for 12 h. The antibacterial effect of the absorbent was examined by observing the inhibition zone.

DFT simulation.

The complex adsorption relationship between adsorbent and uranium was investigated by Density Functional Theory (DFT) calculation, and quantum chemical calculation was performed by ORCA 5.0.2 software. Multiwfn and VMD packages were used to map electrostatic surfaces potential (ESP) of adsorbents, uranium and their complexes. A density-based solvation model was used to simulate the solvent effect. Denotes the minimum potential energy surface of uranium and adsorbent complex[13-15]. We selected a functional polymer with a repeat unit, namely a covalent containing one amidoxime group and one Schiff base, to represent the adsorbent. For uranium, uranyl pentahydrate $[UO_2(H_2O)_5]^{2+}$ was selected, which was dominant in acidic solution[16]. The adsorption energy (E_{ads}) simulating the interaction of uranium with adsorbents was obtained by the formula $E_{ads}=E_t-(E_m+E_U)$. Where E_{ads} (kcal mol^{-1}) is the adsorption energy, E_t (kcal mol^{-1}) is the total electronic energy after adsorption, E_m (kcal mol^{-1}) is the total electronic energy of adsorbent (dimension kcal mol^{-1}), and E_U is the total electronic energy of uranium (kcal mol^{-1}).

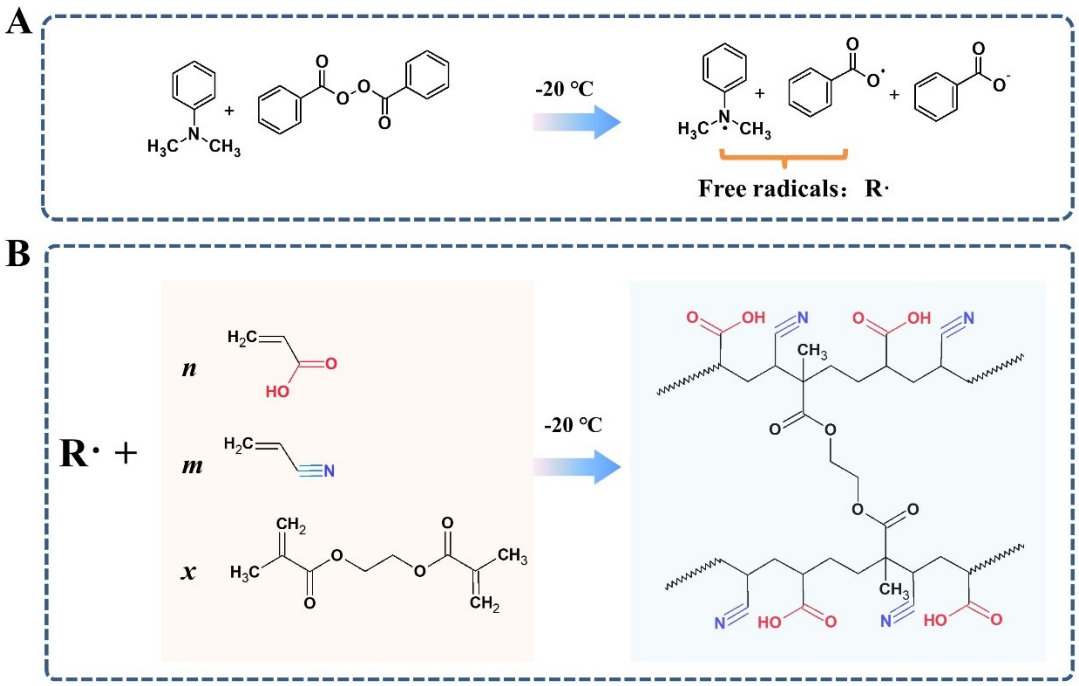

Figure S1. Free radical initiated AA and AN monomers cryo-polymerization. **A**, Redox initiates process that produces free radicals. **B**, Random copolymerization reaction process of monomer and crosslinker initiated by free radicals, where *n*, *m* and *x* represent the number of molecules AA, AN and crosslinker participate in the polymerization reaction, respectively.

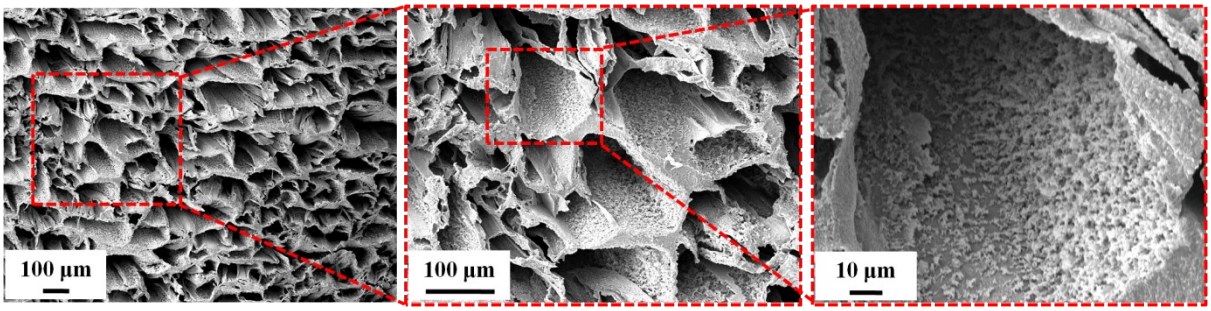

Figure S2. SEM images of PAA-PAN.

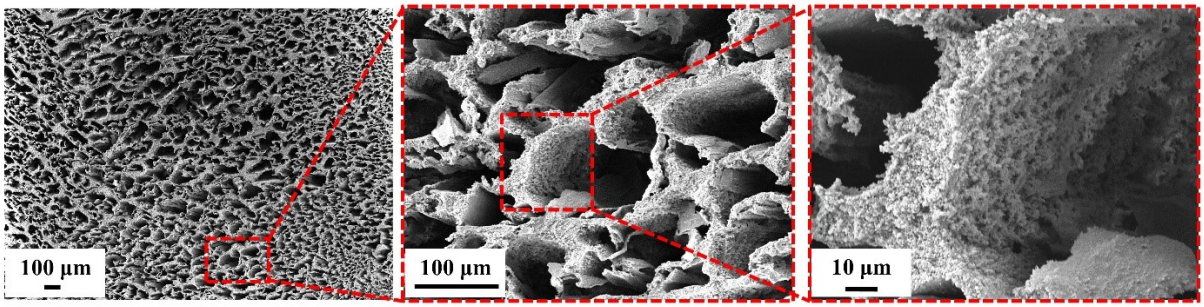

Figure S3. SEM images of PEI-PAA-PAN.

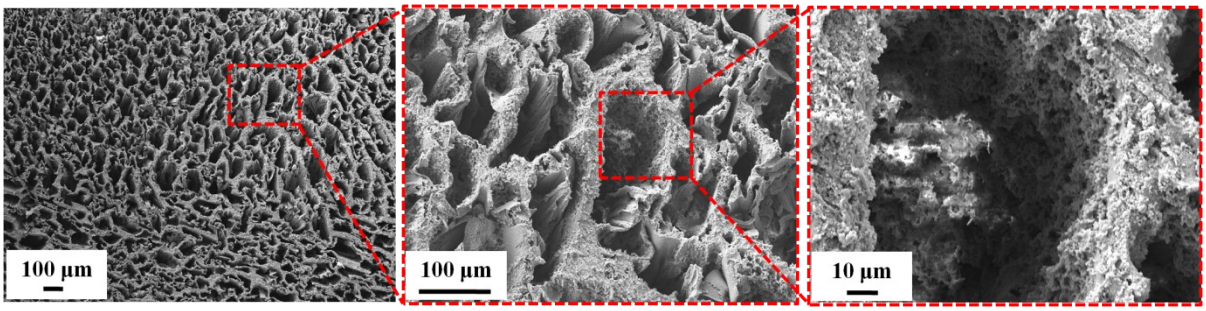

Figure S4. SEM images of sy-PEI-PAA-PAN.

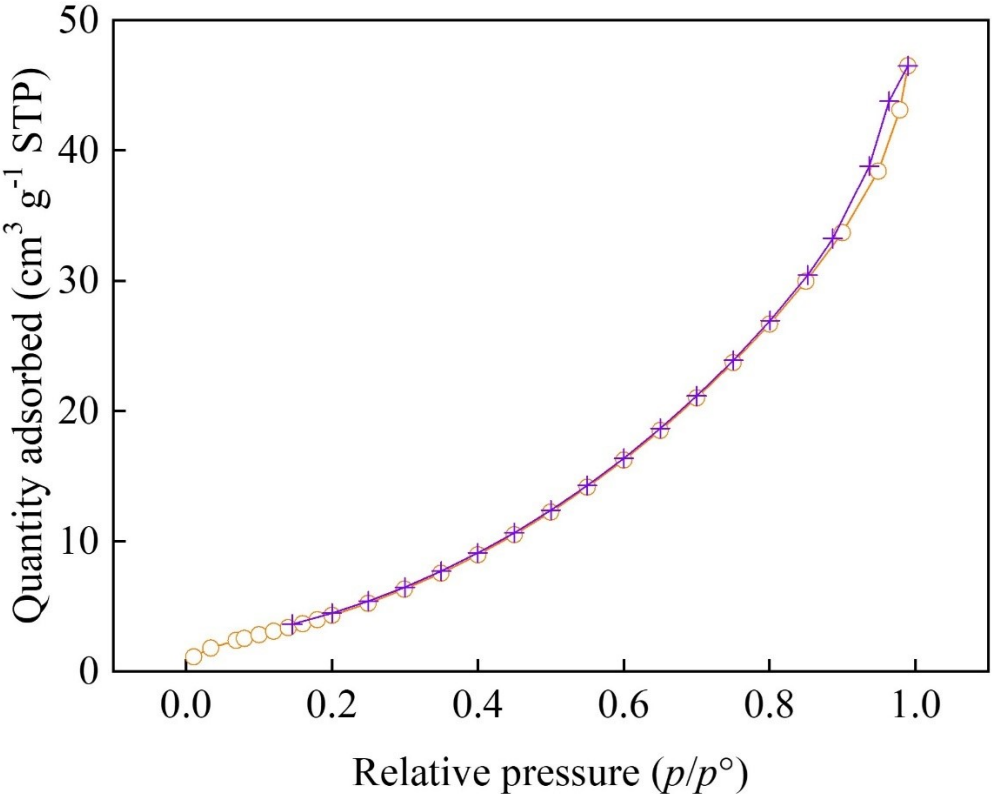

Figure S5. N_2 adsorption/desorption BET test of sy-PEI-PAA-PAO adsorbent at 77.35 K.

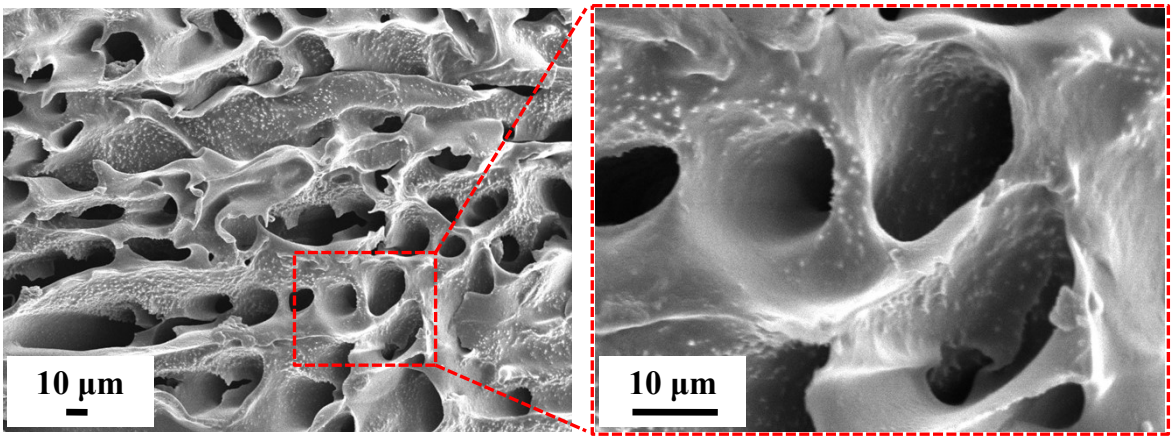

Figure S6. SEM images of sy-PEI-PAA-PAO adsorbent without PU.

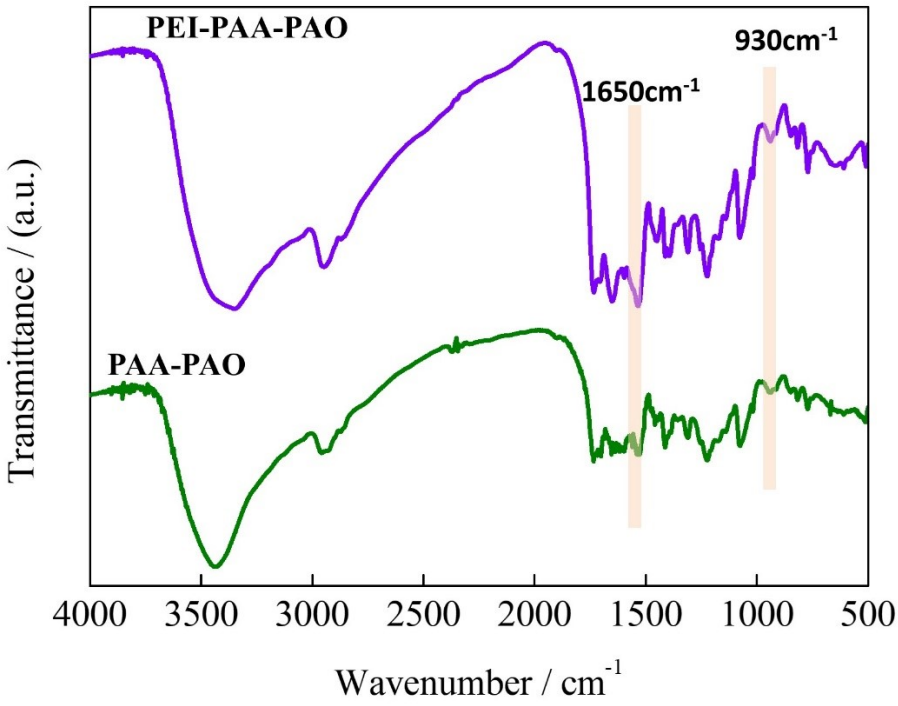

Figure S7. FT-IR characterization of PAA-PAO and PEI-PAA-PAO. The characteristic "C≡N" band was not present, and instead we observed the characteristic peak at 1640 cm^{-1} corresponding to the "C=N" group of the amidoxime group and the characteristic peak at 930 cm^{-1} corresponding to the "N-O" group of the amidoxime group.

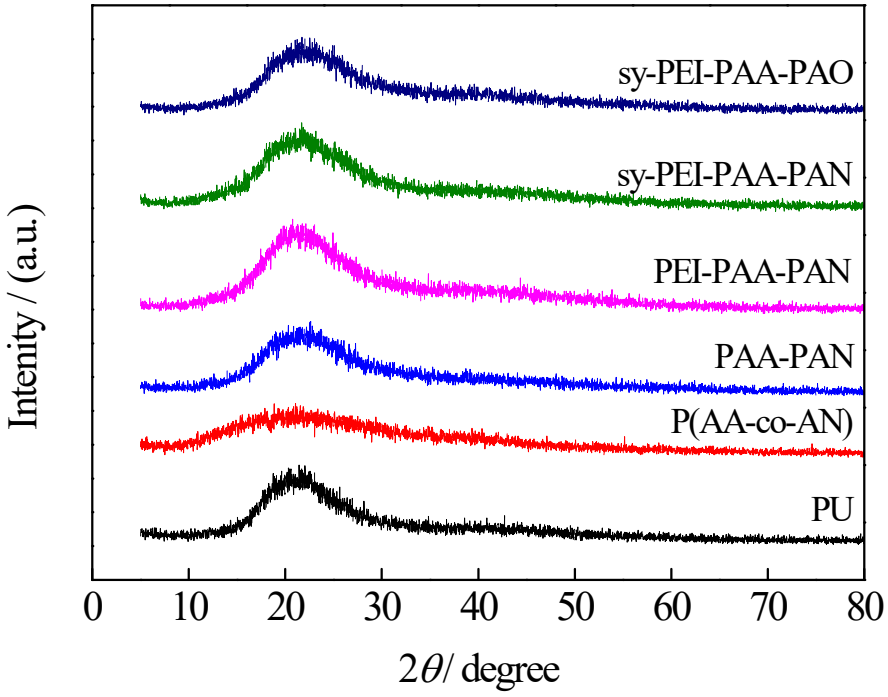

Figure S8. XRD characterization.

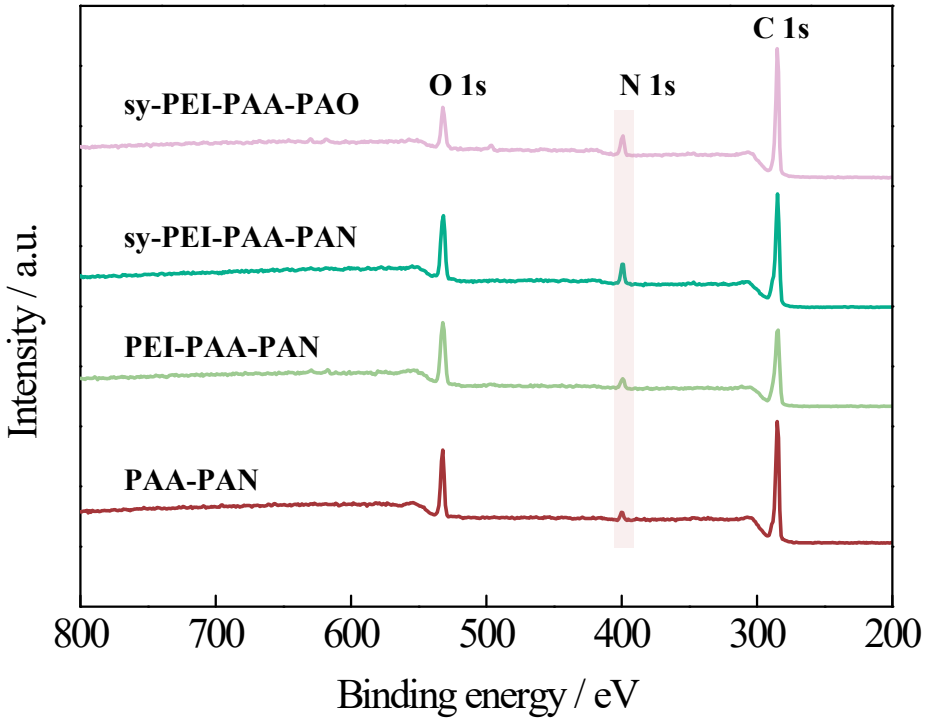

Figure S9. Series of adsorbents correspond to XPS spectra on solid surfaces.

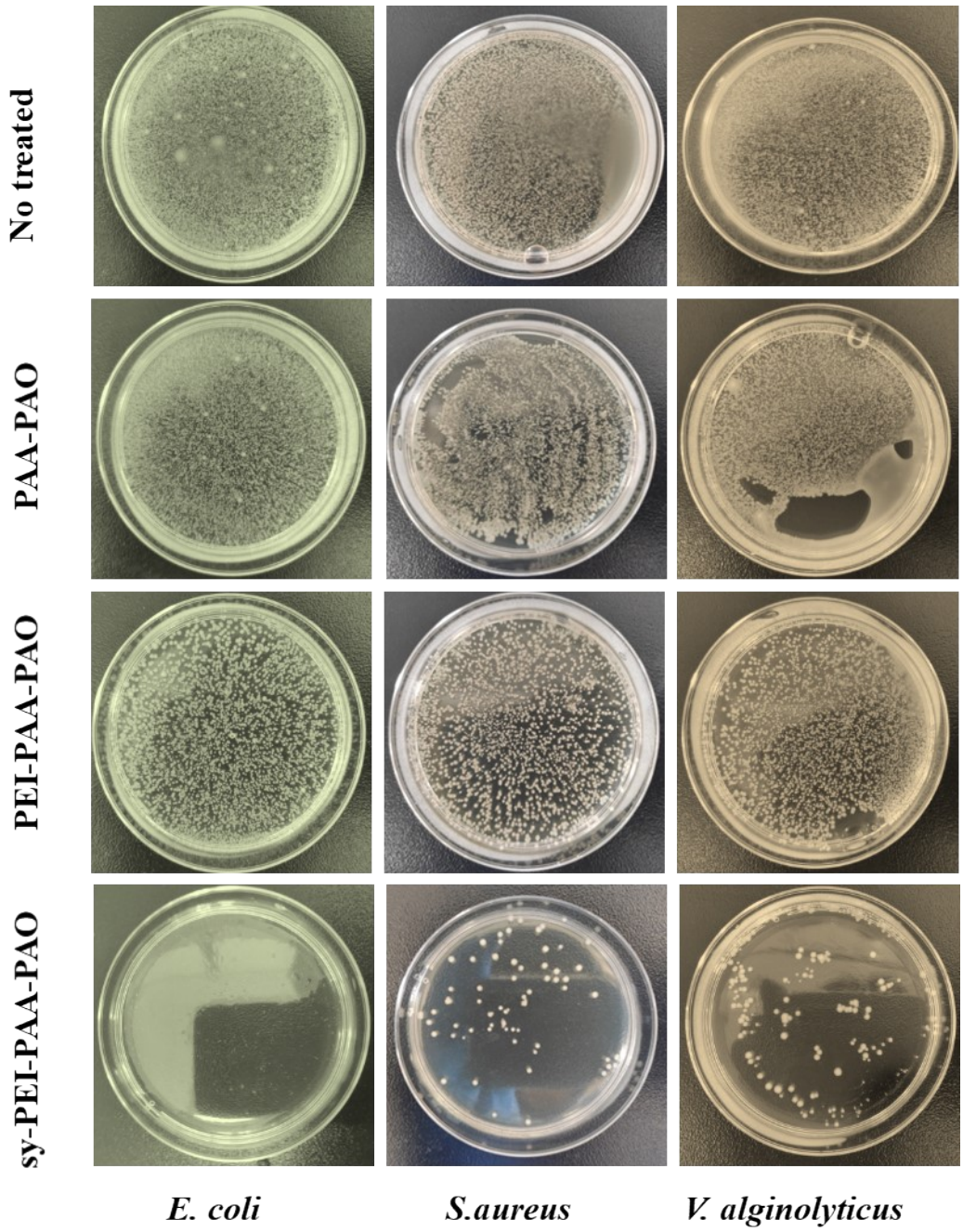

Figure S10. Antibacterial tests corresponding to different adsorbents.

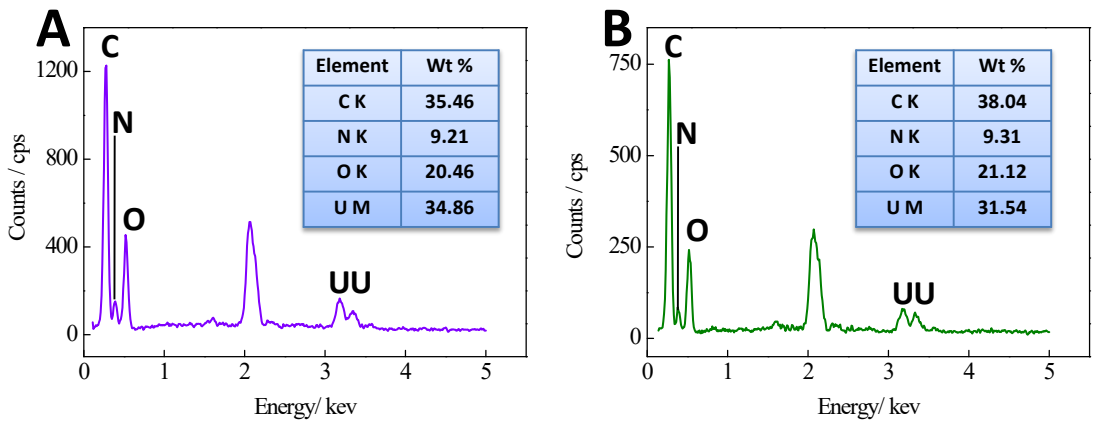

Figure S11. EDS spectra of uranium adsorbed by sy-PEI-PAA-PAO adsorbent. **A**, EDS spectrum of uranium adsorbed on the adsorbent surface. **B**, EDS spectra of uranium adsorbed inside the adsorbent.

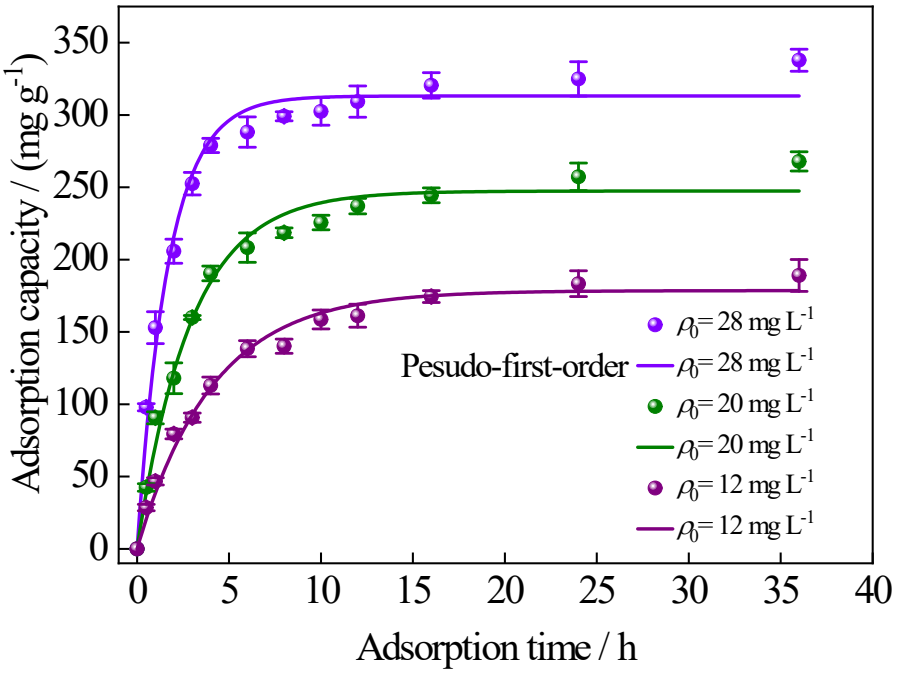

Figure S12. Pseudo-first-order adsorption dynamic model fitting at different initial mass concentrations.

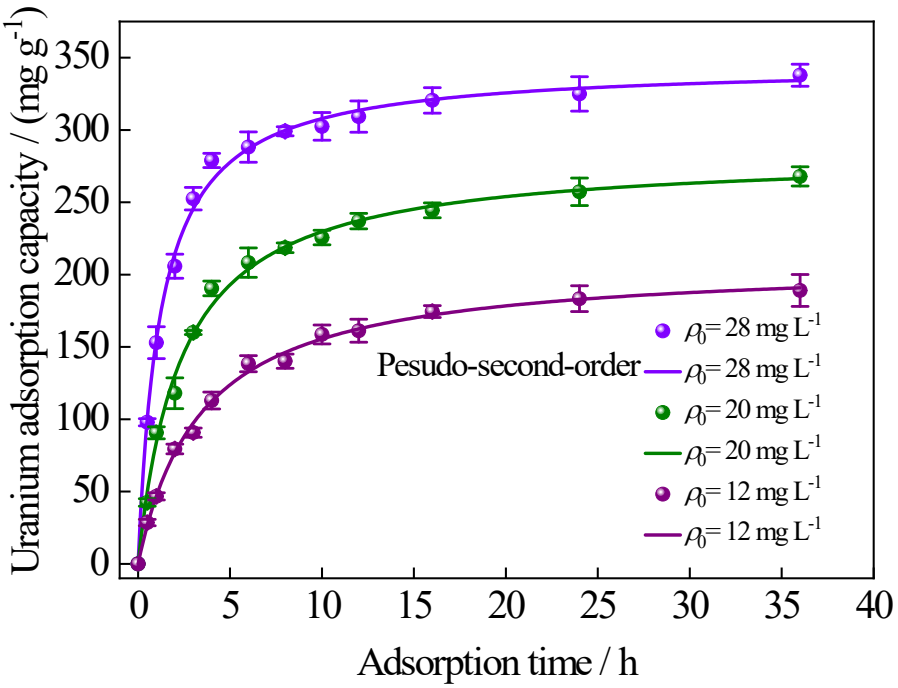

Figure S13. Pseudo-second-order kinetic model fitting under different initial mass concentrations.

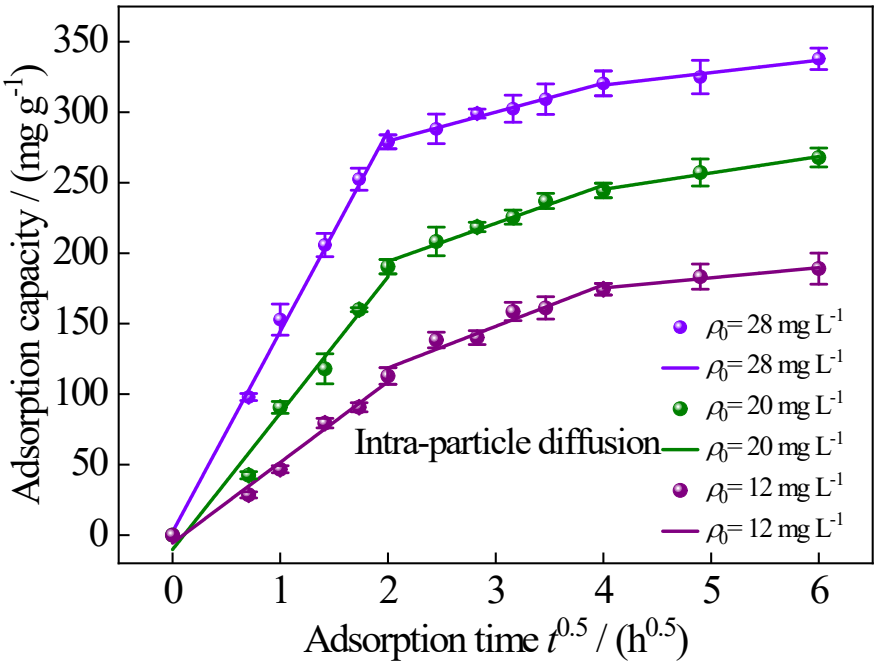

Figure S14. Internal diffusion model fitting.

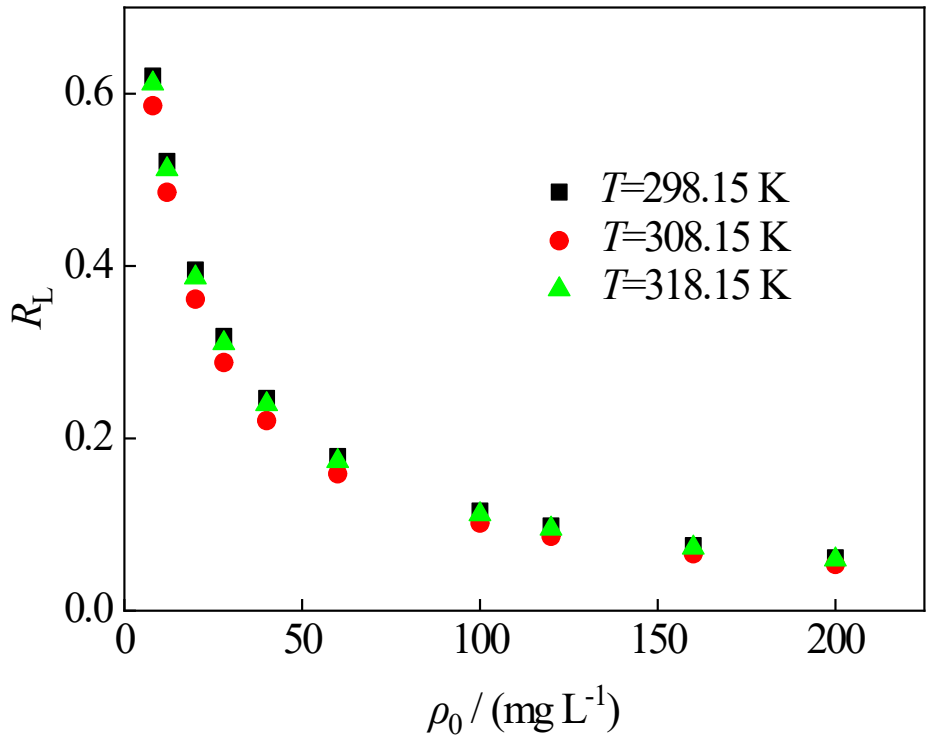

Figure S15. The relationship between R_L and initial uranium mass concentration at different temperatures.

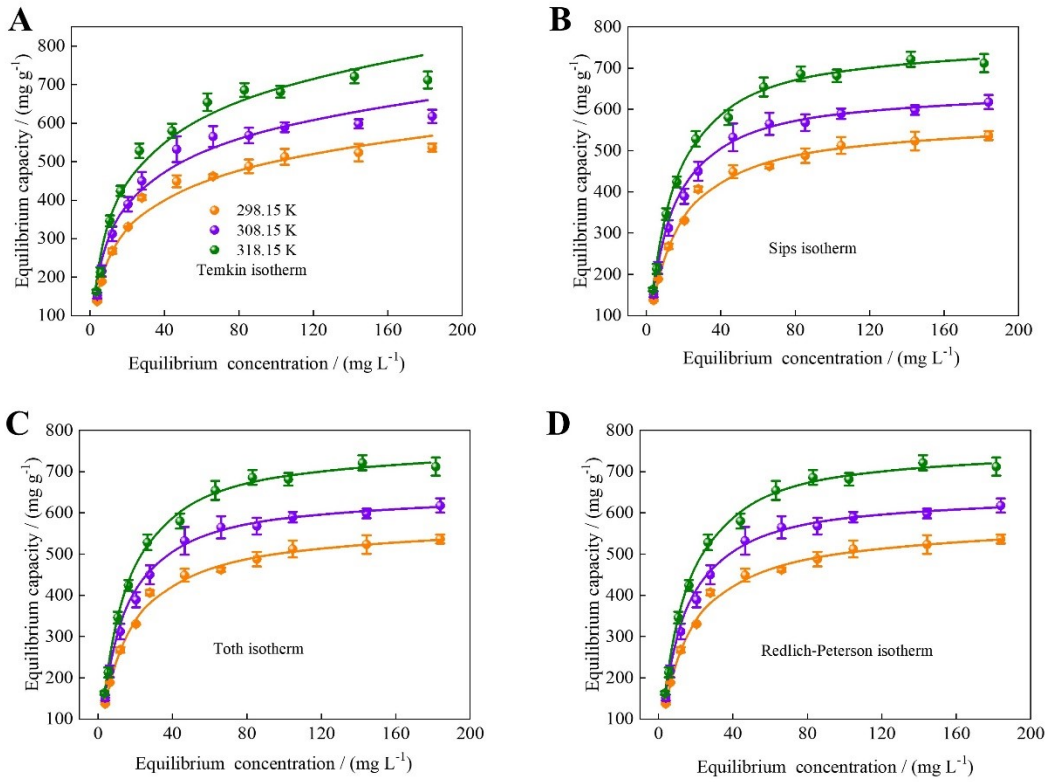

Figure S16. Temkin, Sips, Toth and Redlich-Peterson isotherm models. **A**, Temkin, isotherm models. **B**, Sips isotherm models. **C**, Toth isotherm models. **D**, Redlich-Peterson isotherm models.

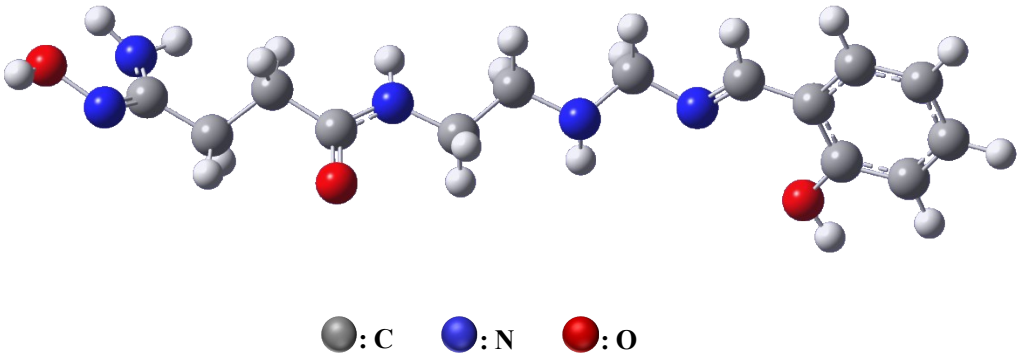

Figure S17. The simplified adsorbent was used to simulate the structure.

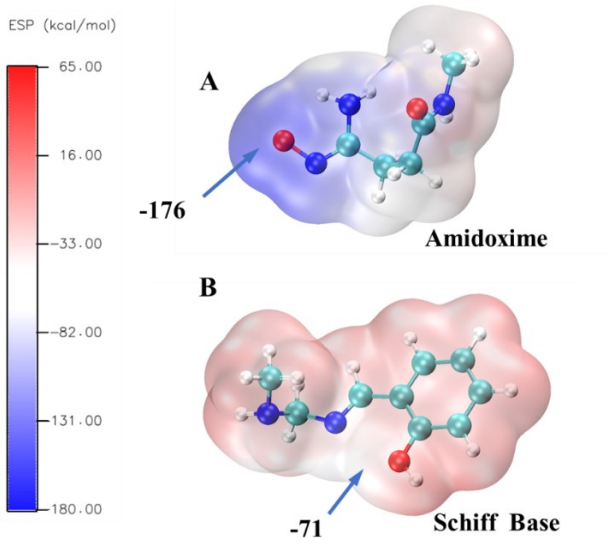

Figure S18. ESP diagram of amidoxime group and Schiff base group. **A**, amidoxime group. **B**, Schiff base group.

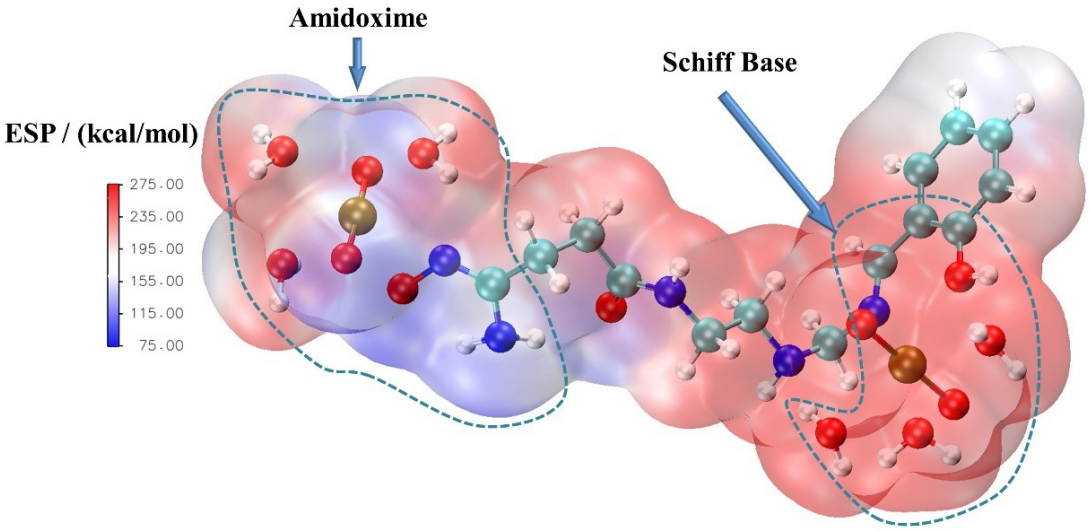

Figure S19. ESP diagram of possible coordination between uranyl ions and adsorbents.

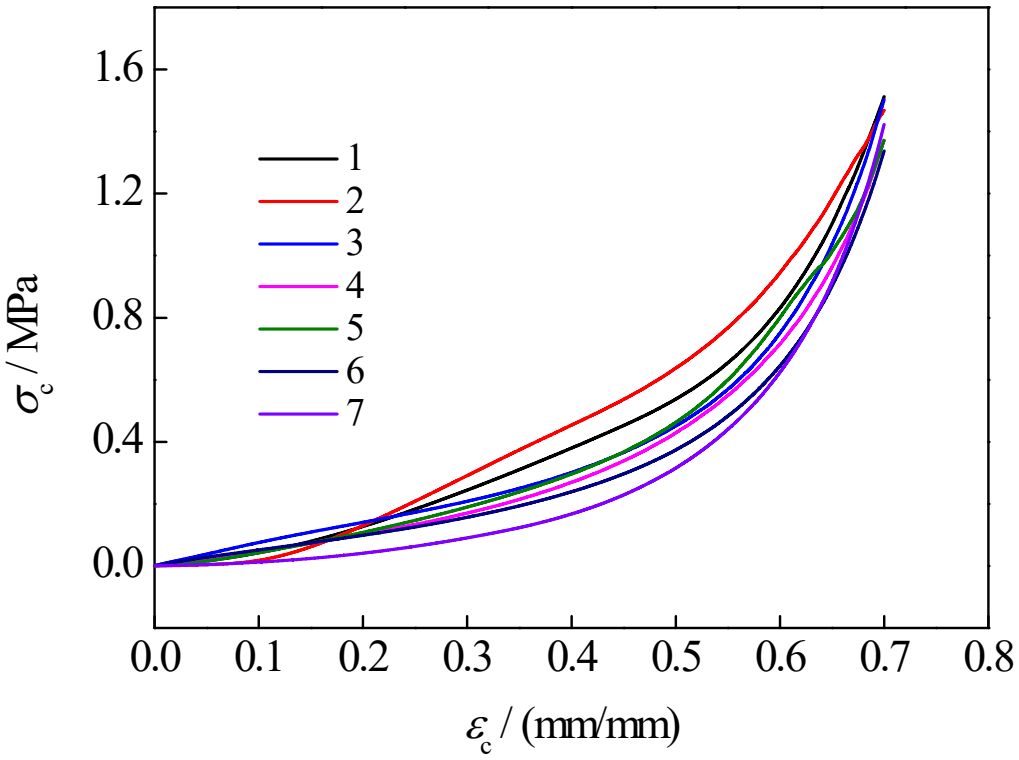

Figure S20. Compressive strength of sy-PEI-PAA-PAO adsorbent [*w*(PU)=5.6 %] after 7 sorption-desorption cycles.

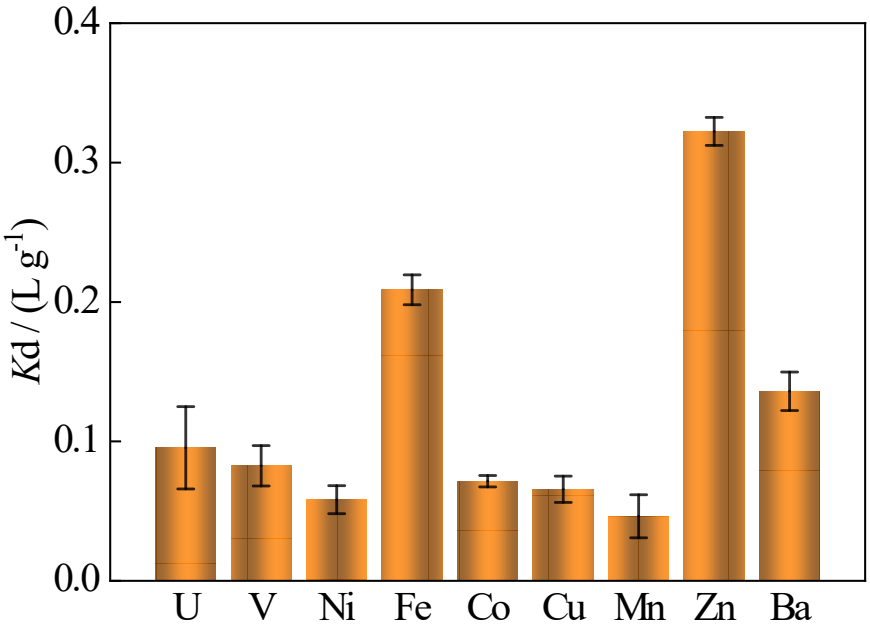

Figure S21. Distribution coefficient K_d and ion species.

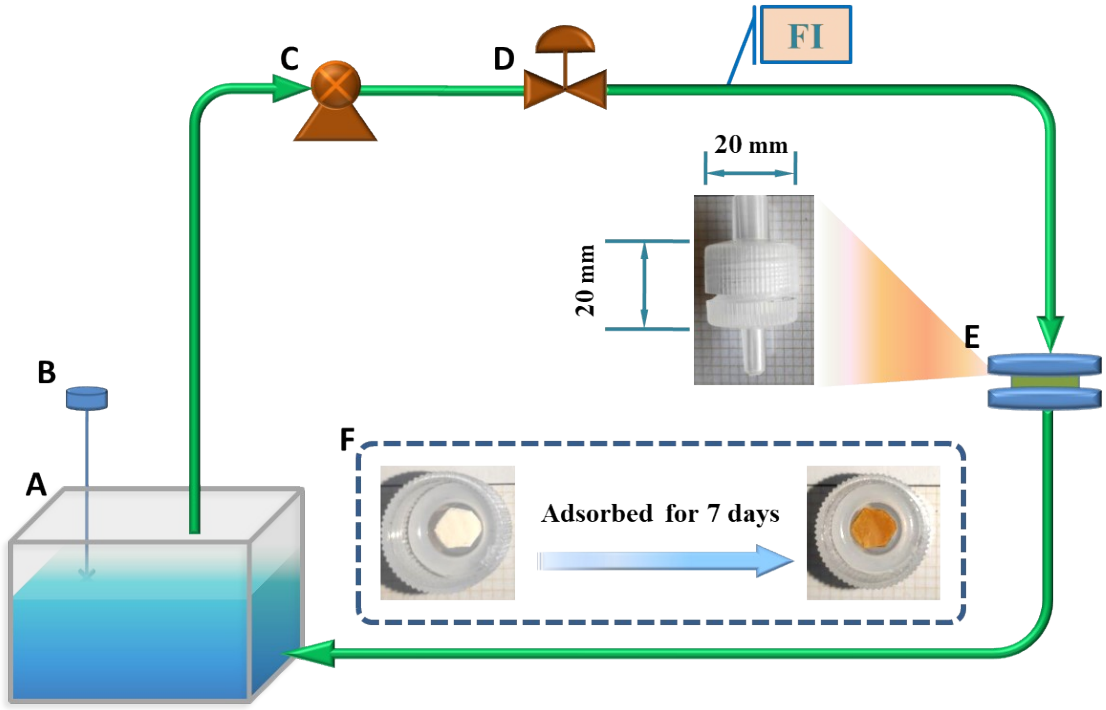

Figure S22. Schematic diagram of natural seawater adsorption. **A**, A natural seawater storage tank. **B**, A blender. **C**, A peristaltic pump. **D**, The valve. **E**, The adsorption column. **F**, Comparison before and after adsorption of adsorbent.

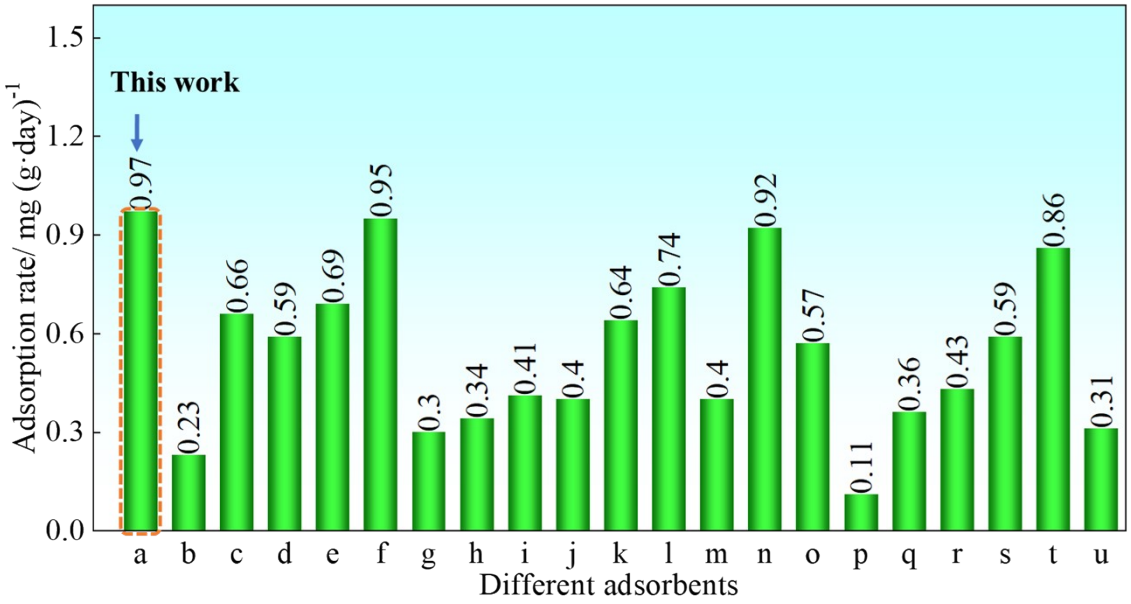

Figure S23. Comparison of average adsorption rates in natural seawater for 7 days, where b ~ u represent the adsorbents according to *ref*.[5, 6, 8, 17-33] and **Table S7**.

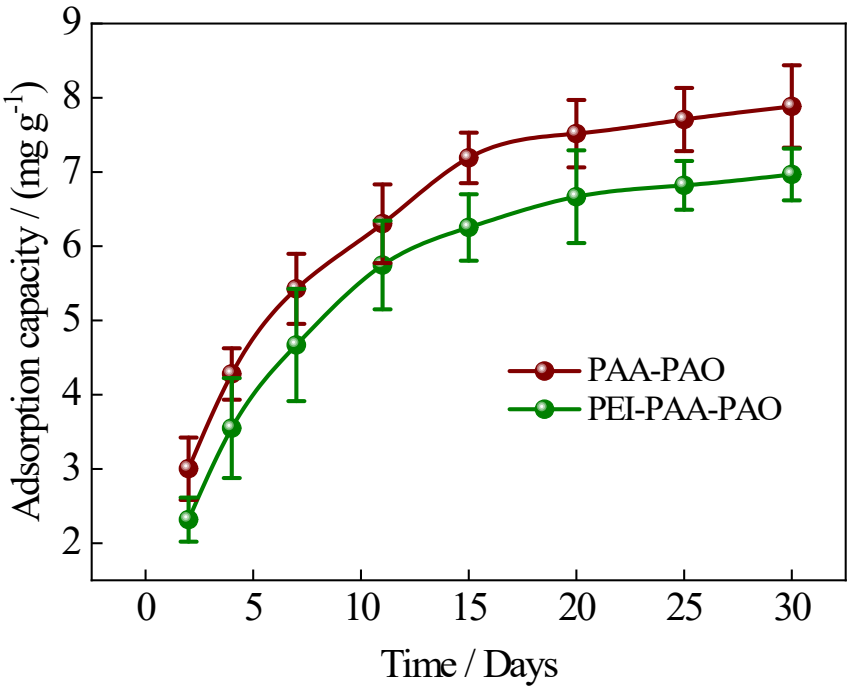

Figure S24. Adsorption of uranium in natural seawater by PAA-PAO and PEI-PAA-PAO.

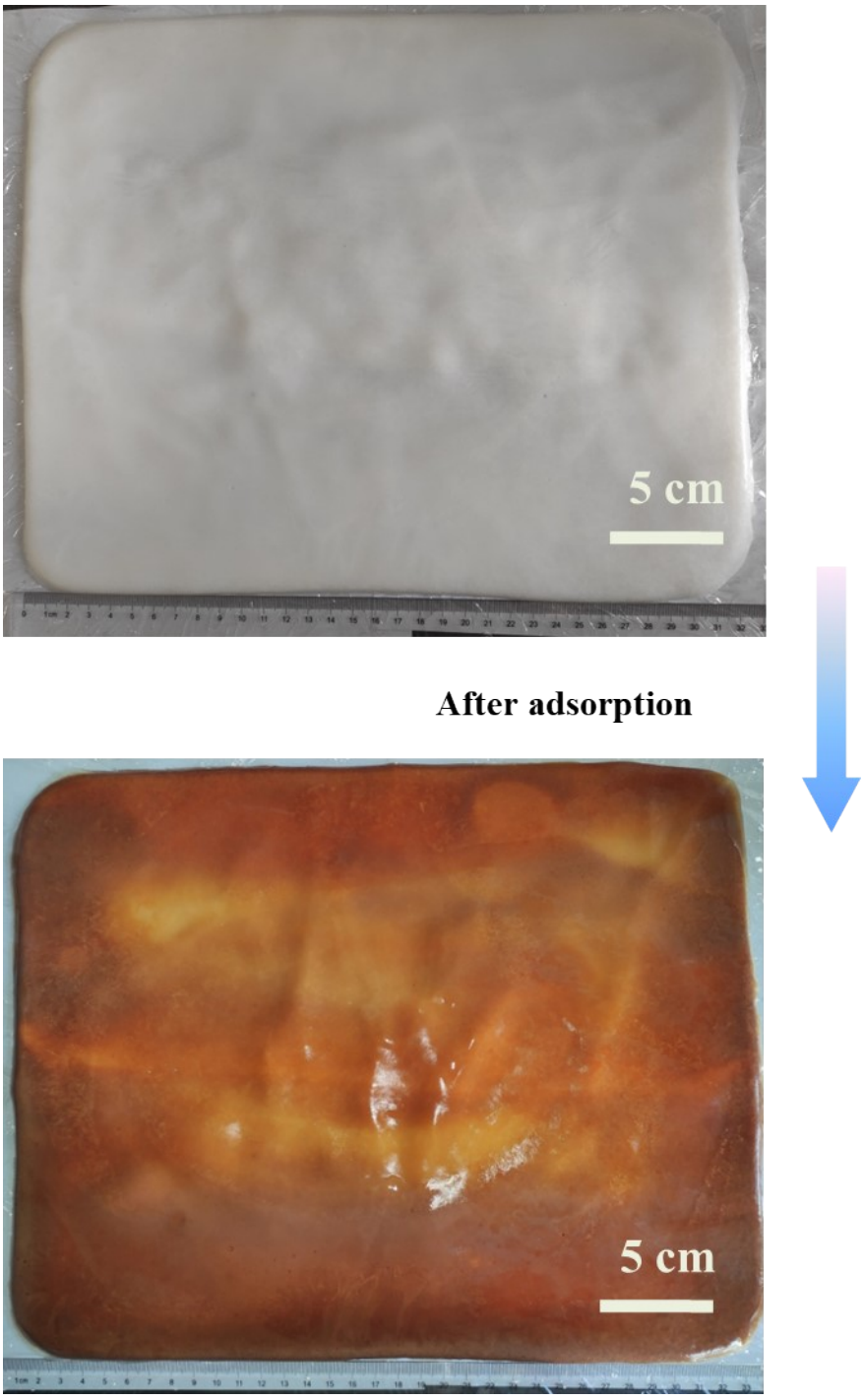

Figure S25. A large-size adsorbent with a size of 33 cm × 28 cm × 0.5 cm and a picture of uranium extraction from seawater were prepared.

Table S1. Mass concentrations corresponding to cryo-crystallization curve experiment.

Numbers	***w*(AA)/ %**	***w*(AN) / %**	***w*(EGD) / %**	***w*(PU)/ %**
r_1	2.73	2.73	0.55	3.40
r_2	3.64	3.64	0.73	4.53
r_3	4.55	4.55	0.91	5.66
r_4	5.45	5.45	1.09	6.79
r_5	6.36	6.36	1.27	7.92

Table S2. Relationship between composition of polymerization system and adsorbent forming.

Numbers	***w*(AA)/ %**	***w*(AN) / %**	***w*(EGD) / %**	***w*(PU)/ %**	***w*(BPO)/ %**	***w*(DMA)/ %**	**Phenomenon**
r_6	3.53	4.53	0.41	4.64	0.06	0.04	No polymerization.
r_7	3.53	4.53	0.41	4.64	0.16	0.11	Partial polymerization, breakage.
r_8	3.53	4.53	0.41	4.64	0.26	0.17	Hierarchical porous structure.
r_9	3.53	4.53	0.41	4.64	0.36	0.24	Hierarchical porous structure.
r_{10}	3.53	4.53	0.41	4.64	0.46	0.31	Hierarchical porous structure.
r_{11}	3.53	4.53	0.41	4.64	0.56	0.37	Polymerized, with few and uneven pores.
r_{12}	3.53	4.53	0.41	4.64	0.66	0.44	Polymerized, poreless gel.

Table S3-1. Results of pseudo first-order model, pseudo second-order model parameter fitting.

ρ_0 (mg L^{-1})	Measured Q_e (mg g^{-1})	Pseudo first order kinetic models			Pseudo second order kinetic models		
		Q_e (mg g-1)	k_1 (h^{-1})	R^2	Q_e (mg g^{-1})	k_2 [g $(mg \cdot h)^{-1}$]	R^2
28	330.57	313.10	0.58	0.979	345.57	2.37×10^{-3}	0.992
20	267.89	247.40	0.34	0.981	283.83	1.48×10^{-3}	0.991
12	188.71	178.60	0.24	0.979	209.14	1.38×10^{-3}	0.991

Table S3-2. Results of intra-particle model parameter fitting.

ρ_0 (mg L^{-1})	Intra-particle models		
	k_p [mg $(g \cdot h^{0.5})^{-1}$]	C (mg g^{-1})	R^2
28	142.20	2.30	0.993
	20.53	238.50	0.992
	8.82	284.00	0.955
20	96.72	-10.24	0.981
	27.03	140.10	0.975
	11.64	198.70	0.987
12	57.24	-5.66	0.984
	29.54	59.47	0.947
	146.5	7.2	0.967

Table S4. Parameter fitting results of isotherm models.

Table S4-1 Langmuir and Freundlich isotherm models

T	Langmuir isotherm model			Freundlich isotherm model		
K	Q_∞ mg g^{-1}	b_L L mg^{-1}	R^2	K_F / $(\mathrm{mg}^{\frac{n-1}{n}} \cdot \mathrm{L}^{\frac{1}{n}}) \cdot \mathrm{g}^{-1}$	n	R^2
298.15	588.23	0.0729	0.989	139.00	3.63	0.914
308.15	654.25	0.0883	0.987	171.20	3.78	0.895
318.15	777.89	0.0793	0.989	184.70	3.54	0.900

Table S4-2 Sips and Toth isotherm models

T	Sips isotherm model				Toth isotherm model			
K	Q_m mg g^{-1}	K_S (L mg^{-1})$^{\alpha}$	α	R^2	K_T mg g^{-1}	a_T (mg L^{-1})$^{\beta}$	β	R^2
298.15	577.71	0.083	0.956	0.995	580.50	10.423	0.934	0.995
308.15	651.79	0.085	1.020	0.998	648.22	12.908	1.039	0.998
318.15	764.66	0.070	1.050	0.994	761.66	16.910	1.090	0.994

Table S4-3 Redlich-Peterson and Temkin isotherm models

T	Redlich-Peterson isotherm model				Temkin isotherm model		
K	K_{RP} L g^{-1}	a_{RP} (L mg^{-1})$^{\gamma}$	γ	R^2	A L mg^{-1}	b (J·g) (mol·mg)$^{-1}$	R^2
298.15	45.61	0.087	0.983	0.995	1.062	23.05	0.976
308.15	56.05	0.081	1.011	0.998	1.270	21.13	0.970
318.15	58.39	0.070	1.020	0.993	1.050	17.83	0.971

Table S5. ESP simulation results of uranium interaction with adsorbent.

Coordination mode	E_{ads} **(kcal mol^{-1})**
U-sy-PEI-PAA-PAO(E)	-16.08
U-sy-PEI-PAA-PAO(F)	-45.93
U-sy-PEI-PAA-PAO(G)	-37.53
U-sy-PEI-PAA-PAO(H)	-35.99

Note: E, F, G and H correspond to the adsorption form in **Fig. 5**, respectively

Table S6. Initial ion species and concentration in selectivity experiment of multi-ion adsorption.

Elements types		**U**	**V**	**Ni**	**Fe**	**Co**	**Cu**	**Mn**	**Zn**	**Ba**
Initial concentration (mg L^{-1})	1#	0.3348	0.2574	0.0943	0.2781	0.082	0.1423	0.0756	0.4562	0.1765
	2#	0.3219	0.2234	0.0912	0.2864	0.078	0.1367	0.0735	0.4123	0.1678
	3#	0.3402	0.2457	0.0829	0.2686	0.081	0.1396	0.0712	0.4432	0.1628
Average value (mg L^{-1})		0.3323	0.2422	0.0895	0.2777	0.0803	0.1395	0.0734	0.4372	0.1691

Table S7. Comparison of the current adsorbent with previously reported 3D porous adsorbents with similar pore sizes.

Codes from Fig. S23	Names	Forming	Pore forming methods	Pore range	Adsorption time / Days	Mass of Adsorbents	Seawater dosage	Seawater source	Capacities (mg g^{-1})	*Ref.*
a	sy-PEI-PAA-PAO	3D hierarchical porous adsorbent	Cryo-polymerization	10 ~ 100 μm ~ 1 μm	30	20 mg	200 L	East China Sea	10.45	This work
b	MS@PIDO/Alg	Hybrid sponge	Commercially available melamine sponge as the base	100 ~200 μm	56	Not mentioned	5 T	Boundary Island of the South China Sea	5.84	[17]
c	Anti-PAO	Aerogels	Freeze-drying	10 μm	30	Not mentioned	1 T	South China Sea	9.29	[18]
d	NC-PAO DN	Double-Network hydrogel	Not mentioned	20 ~ 50 μm	25	12 columns × 5 mg	1 T	South China Sea	8.62	[19]
e	Zn^{2+} – PAO	Supramolecular Hydrogel	Freeze-drying	10 ~ 20 μm Nano scale of pore after adsorption	28	12 columns × 3 mg	1 T	South China Sea	9.23	[5]
f	AO-PIM	Hierarchica porous membrane	Water as a coagulation bath	20 μm; 300 ~500 nm	28	10 mg	100 L	Yellow Sea, Tsingtao, China	9.03	[6]
g	CP–PAO	Composite hydrogel	Freeze-drying	10 μm After the adsorption 50 nm	42	12 columns × 3 mg	1 T	South China Sea	6.21	[20]
h	BP@CNF-MOF	Nanofiber Aerogel	Freeze-drying	10 ~100 μm	42	100 mg	100 L	South China Sea	6.77	[21]
i	UiO-66-NH2	Carbon	Commercially	110 μm	30	100 mg	100 L	South China Sea	5.52	[22]

	@CS-PDA	sponge	available melamine sponge as the base							
j	SMON–PAO	Porous Nanofiber	leaching in water	10~300 nm	56	10 mg	1 T	South China Sea	9.59	[23]
k	PAO PNM	Porous network membranes	Water as a coagulation bath	100 nm	35	12 columns × 3 mg	1 T	South China Sea	9.35	[24]
l	PPH-OP	Hydrogel	Freezing-dry	1 μm	21	10 mg	100 L	the west coast of Haikou City, China	7.5	[25]
m	PAO semi-IPN	Hydrogel Membrane	Freezing-dry	5 ~10μm After the adsorption 50~100 nm	28	12 columns × 3 mg	1 T	South China Sea	4.87	[8]
n	DC-PAO	Hydrogel	Bottom liquid nitrogen induction	20μm	7	30 mg	100 kg	Qiongzhou strait nearby the Haikou city of Hainan , China	6.42	[26]
o	PAO-Co	Particle	Freeze drying	~5μm	49	10 mg	100 L	South China Sea	9.7	[27]
p	Anti-LS/SA	Adhesive sponges	Freeze-drying	~26 μm	30	8 mg	100 L	South China Sea	2.2	[28]
q	HA-PAO NFMs	Nanofiber membranes	Not mentioned	0.5 ~ 5μm	28	10 mg	100 L	South China Sea	6.73	[29]
r	CMPM	Aligned microchannel aerogel	Raw wood etching	50 μm	30	100 mg	100 L	Qiongzhou strait nearby the Haikou city of Hainan , China	5.81	[30]
s	Fe@PDA-PAO	Hydrogel	Not mentioned	10 μm	42	100 mg	100 L	Qiongzhou strait	12.31	[31]

		membrane						nearby the Haikou city of Hainan , China		
t	VA-PG	Hybrid Sheets′ Membrane	Freeze-drying	5 ~10 μm	32	100 mg	100 L	Qiongzhou strait nearby the Haikou city of Hainan , China	13.63	[32]
u	AOOBCH	Aligned microchannel aerogel	Raw bamboo etching	~10 μm	30	5 mg	10 L	Not mentioned	6.37	[33]

References for electronic supplementary information

1 X. Xu, H. Zhang, J. Ao, L. Xu, X. Liu, X. Guo, J. Li, L. Zhang, Q. Li, X. Zhao, B. Ye, D. Wang, F. Shen and H. Ma, 3D hierarchical porous amidoxime fibers speed up uranium extraction from seawater, *Energ. Environ. Sci.*, 2019, **12**, 1979-1988.

2 T. Sedlačík, T. Nonoyama, H. Guo, R. Kiyama, T. Nakajima, Y. Takeda, T. Kurokawa and J. P. Gong, Preparation of Tough Double- and Triple-Network Supermacroporous Hydrogels through Repeated Cryogelation, *Chem. Mat.*, 2020, **32**, 8576-8586.

3 Z. Huang, H. Dong, N. Yang, H. Li, N. He, X. Lu, J. Wen and X. Wang, Bifunctional Phosphorylcholine-Modified Adsorbent with Enhanced Selectivity and Antibacterial Property for Recovering Uranium from Seawater, *ACS Appl. Mater. Interfaces*, 2020, **12**, 16959-16968.

4 W. Cui, C. Zhang, R. Liang and J. Qiu, Covalent organic framework hydrogels for synergistic seawater desalination and uranium extraction, *J. Mater. Chem. A*, 2021, **9**, 25611-25620.

5 B. Yan, C. Ma, J. Gao, Y. Yuan and N. Wang, An Ion‐Crosslinked Supramolecular Hydrogel for Ultrahigh and Fast Uranium Recovery from Seawater, *Adv. Mater.*, 2020, **32**, 1906615.

6 L. Yang, H. Xiao, Y. Qian, X. Zhao, X. Kong, P. Liu, W. Xin, L. Fu, L. Jiang and L. Wen, Bioinspired hierarchical porous membrane for efficient uranium extraction from seawater, *Nat. Sustain.*, 2022, **5**, 71-80.

7 H. Li, N. He, C. Cheng, H. Dong, J. Wen and X. Wang, Antimicrobial polymer contained adsorbent: A promising candidate with remarkable anti-biofouling ability and durability for enhanced uranium extraction from seawater, *Chem. Eng. J.*, 2020, **388**, 124273.

8 C. Ma, J. Gao, D. Wang, Y. Yuan, J. Wen, B. Yan, S. Zhao, X. Zhao, Y. Sun, X. Wang and N. Wang, Sunlight Polymerization of Poly(amidoxime) Hydrogel Membrane for Enhanced Uranium Extraction from Seawater, *Adv. Sci.*, 2019, 1900085.

9 X. Guo, H. Yang, Q. Liu, J. Liu, R. Chen, H. Zhang, J. Yu, M. Zhang, R. Li and J. Wang, A chitosan-graphene oxide/ZIF foam with anti-biofouling ability for uranium recovery from seawater, *Chem. Eng. J.*, 2020, **382**, 122850.

10 X. Xu, L. Xu, J. Ao, Y. Liang, C. Li, Y. Wang, C. Huang, F. Ye, Q. Li, X. Guo, J. Li, H. Wang, S. Ma and H. Ma, Ultrahigh and economical uranium extraction from seawater *via* interconnected open-pore architecture poly(amidoxime) fiber, *J. Mater. Chem. A*, 2020, **8**, 22032-22044.

11 S. Zhao, Y. Yuan, Q. Yu, B. Niu, J. Liao, Z. Guo and N. Wang, A Dual‐Surface Amidoximated Halloysite Nanotube for High‐Efficiency Economical Uranium Extraction from Seawater, *Angew. Chem. Int Edit.*, 2019, **58**, 14979-14985.

12 H. Pan, L. Kuo, C. M. Wai, N. Miyamoto, R. Joshi, J. R. Wood, J. E. Strivens, C. J. Janke, Y. Oyola, S. Das, R. T. Mayes and G. A. Gill, Elution of Uranium and Transition Metals from Amidoxime-Based Polymer Adsorbents for Sequestering Uranium from Seawater, *Ind. Eng. Chem. Res.*, 2016, **55**, 4313-4320.

13 T. Lu and F. Chen, Multiwfn: A multifunctional wavefunction analyzer, *J. Comput. Chem.*, 2011, **33**, 580-592.

14 W. Humphrey, A. Dalke and K. Schulten, VMD: Visual molecular dynamics, *J. Mol. Graphics.*, 1996, **14**, 33-38.

15 C. Lee, W. Yang and R. G. Parr, Development of the Colle-Salvetti correlation-energy formula into a functional of the electron density, *Phys. Rev. B*, 1988, **37**, 785-789.

16 E. Grabias and M. Majdan, A DFT study of uranyl hydroxyl complexes: structure and stability of trimers and tetramers, *J. Radioanal. Nucl. Chem.*, 2017, **313**, 455-465.

17 D. Wang, J. Song, S. Lin, J. Wen, C. Ma, Y. Yuan, M. Lei, X. Wang, N. Wang and H. Wu, A Marine-Inspired Hybrid Sponge for Highly Efficient Uranium Extraction from Seawater, *Adv. Funct. Mater.*, 2019, **29**, 1901009.

18 S. Shi, B. Li, Y. Qian, P. Mei and N. Wang, A simple and universal strategy to construct robust and anti-biofouling amidoxime aerogels for enhanced uranium extraction from seawater, *Chem. Eng. J.*, 2020, **397**, 125337.

19 R. Liu, S. Wen, Y. Sun, B. Yan, J. Wang, L. Chen, S. Peng, C. Ma, X. Cao, C. Ma, G. Duan, S. Shi, Y. Yuan and N. Wang, A nanoclay enhanced Amidoxime-Functionalized Double-Network hydrogel for fast and massive uranium recovery from seawater, *Chem. Eng. J.*, 2021, **422**, 130060.

20 J. Gao, Y. Yuan, Q. Yu, B. Yan, Y. Qian, J. Wen, C. Ma, S. Jiang, X. Wang and N. Wang, Bio-inspired antibacterial cellulose paper–poly(amidoxime) composite hydrogel for highly efficient uranium(Ⅵ) capture from seawater, *Chem. Commun.*, 2020, **56**, 3935-3938.

21 M. Chen, T. Liu, X. Zhang, R. Zhang, S. Tang, Y. Yuan, Z. Xie, Y. Liu, H. Wang, K. V. Fedorovich and N. Wang, Photoinduced Enhancement of Uranium Extraction from Seawater by MOF/Black Phosphorus Quantum Dots Heterojunction Anchored on Cellulose Nanofiber Aerogel, *Adv. Funct. Mater.*, 2021, **31**, 2100106.

22 T. Liu, X. Zhang, H. Wang, M. Chen, Y. Yuan, R. Zhang, Z. Xie, Y. Liu, H. Zhang and N. Wang, Photothermal enhancement of uranium capture from seawater by monolithic MOF-bonded carbon sponge, *Chem. Eng. J.*, 2021, **412**, 128700.

23 Y. Yuan, S. Zhao, J. Wen, D. Wang, X. Guo, L. Xu, X. Wang and N. Wang, Rational Design of Porous Nanofiber Adsorbent by Blow-Spinning with Ultrahigh Uranium Recovery Capacity from Seawater, *Adv. Funct. Mater.*, 2018, **29**, 1805380.

24 S. Shi, Y. Qian, P. Mei, Y. Yuan, N. Jia, M. Dong, J. Fan, Z. Guo and N. Wang, Robust flexible poly(amidoxime) porous network membranes for highly efficient uranium extraction from seawater, *Nano Energy*, 2020, **71**, 104629.

25 Y. Yuan, Q. Yu, M. Cao, L. Feng, S. Feng, T. Liu, T. Feng, B. Yan, Z. Guo and N. Wang, Selective extraction of uranium from seawater with biofouling-resistant polymeric peptide, *Nat. Sustain.*, 2021, **4**, 708-714.

26 N. Wang, X. Zhao, J. Wang, B. Yan, S. Wen, J. Zhang, K. Lin, H. Wang, T. Liu, Z. Liu, C. Ma, J. Li and Y. Yuan, Accelerated Chemical Thermodynamics of Uranium Extraction from Seawater by Plant‐Mimetic Transpiration, *Adv. Sci.*, 2021, **8**, 2102250.

27 W. Sun, L. Feng, J. Zhang, K. Lin, H. Wang, B. Yan, T. Feng, M. Cao, T. Liu, Y. Yuan and N. Wang, Amidoxime Group‐Anchored Single Cobalt Atoms for Anti‐Biofouling during Uranium Extraction from Seawater, *Adv. Sci.*, 2022, **9**, 2105008.

28 P. Mei, R. Wu, S. Shi, B. Li, C. Ma, B. Hu, Y. Yuan, H. Wang, T. Liu and N. Wang, Conjugating hyaluronic acid with porous biomass to construct anti-adhesive sponges for rapid uranium extraction from seawater, *Chem. Eng. J.*, 2021, **420**, 130382.

29 S. Shi, R. Wu, S. Meng, G. Xiao, C. Ma, G. Yang and N. Wang, High-strength and anti-biofouling nanofiber membranes for enhanced uranium recovery from seawater and wastewater, *J. Hazard. Mater.*, 2022, **436**, 128983.

30 T. Liu, X. Zhang, A. Gu, Y. Liu, M. Chen, H. Wang, R. Zhang, S. Tang, Z. Xie and N. Wang, In-situ grown bilayer MOF from robust wood aerogel with aligned microchannel arrays toward

selective extraction of uranium from seawater, *Chem. Eng. J.*, 2022, **433**, 134346.

31 T. Liu, Z. Xie, M. Chen, S. Tang, Y. Liu, J. Wang, R. Zhang, H. Wang, X. Guo, A. Gu, Y. Yuan and N. Wang, Mussel-inspired dual-crosslinked polyamidoxime photothermal hydrogel with enhanced mechanical strength for highly efficient and selective uranium extraction from seawater, *Chem. Eng. J.*, 2022, **430**, 133182.

32 T. Liu, R. Zhang, M. Chen, Y. Liu, Z. Xie, S. Tang, Y. Yuan and N. Wang, Vertically Aligned Polyamidoxime/Graphene Oxide Hybrid Sheets' Membrane for Ultrafast and Selective Extraction of Uranium from Seawater, *Adv. Funct. Mater.*, 2021, **32**, 2111049.

33 Y. Wang, Z. Lin, H. Zhang, Q. Liu, J. Yu, J. Liu, R. Chen, J. Zhu and J. Wang, Anti-bacterial and super-hydrophilic bamboo charcoal with amidoxime modified for efficient and selective uranium extraction from seawater, *J. Colloid Interface Sci.*, 2021, **598**, 455-463.